

## Programmable graphene doping via electron beam irradiation

Yangbo Zhou<sup>1</sup>, Jakub Jadwiszczak<sup>1</sup>, Darragh Keane<sup>1</sup>, Ying Chen<sup>2</sup>, Dapeng Yu<sup>3</sup>,

Hongzhou Zhang<sup>1</sup>

<sup>1</sup>*School of Physics and CRANN, Trinity College Dublin, Dublin 2, Ireland*

<sup>2</sup>*Institute for Frontier Materials, Deakin University, Waurn Ponds, VIC 3216, Australia*

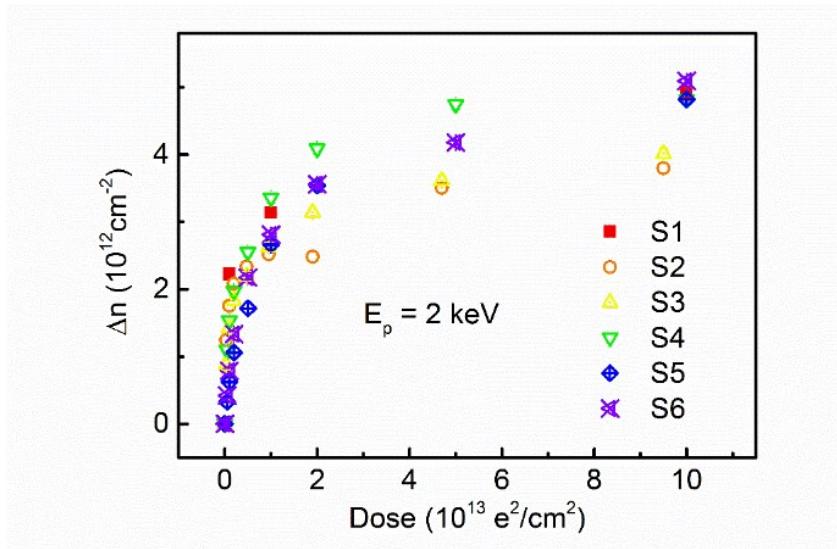
<sup>3</sup>*School of Physics, Peking University, Beijing, 100871, China*

### 1. Reproducibility and controllability of electron beam induced doping

We demonstrate the reproducibility of the electron beam (e-beam) induced doping by investigating six similar monolayer graphene field-effect transistor (FET) devices, which were fabricated on different substrates made from the same material. Henceforth, we will not mention their thickness as it is understood the devices consist of atomically thin graphene. Fig. S1 shows their responses to the e-beam doping, i.e. the dependence of the doping level as a function of the dose delivered by a 2 keV beam with 20 pA beam current. The dose ranged from  $10^{12} e^- / cm^2$  to  $10^{14} e^- / cm^2$ . All the six devices exhibit the same doping behavior as shown in the inset of Fig. 1 (c) in the main manuscript and the carrier density change ( $\Delta n$ ) saturates at a value close to  $4.5 \times 10^{12} cm^{-2}$ . The small variation in the saturated density across these devices may be due to the variation in the quality of the substrates (see section 6 for detailed discussion).

Fig. S2 shows the gate responses of a graphene FET under the irradiation of focused electron beams with energies from 1 keV to 5 keV, and corresponding doses of  $10^{12} e^- / cm^2$ ,  $10^{13} e^- / cm^2$  and  $10^{14} e^- / cm^2$  respectively. The results show that for these beam energies,

the gate curves shift to the left after irradiation, indicating n-type doping in graphene. Among these beam energies, the 2keV beam induces the largest shift of the Dirac point at all doses (Fig. S3). This can be attributed to the fact that the 1 keV e-beam will generate a larger surface potential which causes a faster reduction of secondary electron (SE) yield; thus a



lower saturated doping (see Section 5).

**Fig. S1** The change of electron carrier density  $\Delta n$  as a function of beam dose for six different graphene devices.  $\Delta n$  is defined as the change of carrier densities at 0 V back-gate, which is calculated from the shifts of Dirac points in the corresponding  $\sigma(V_g)$  plots.

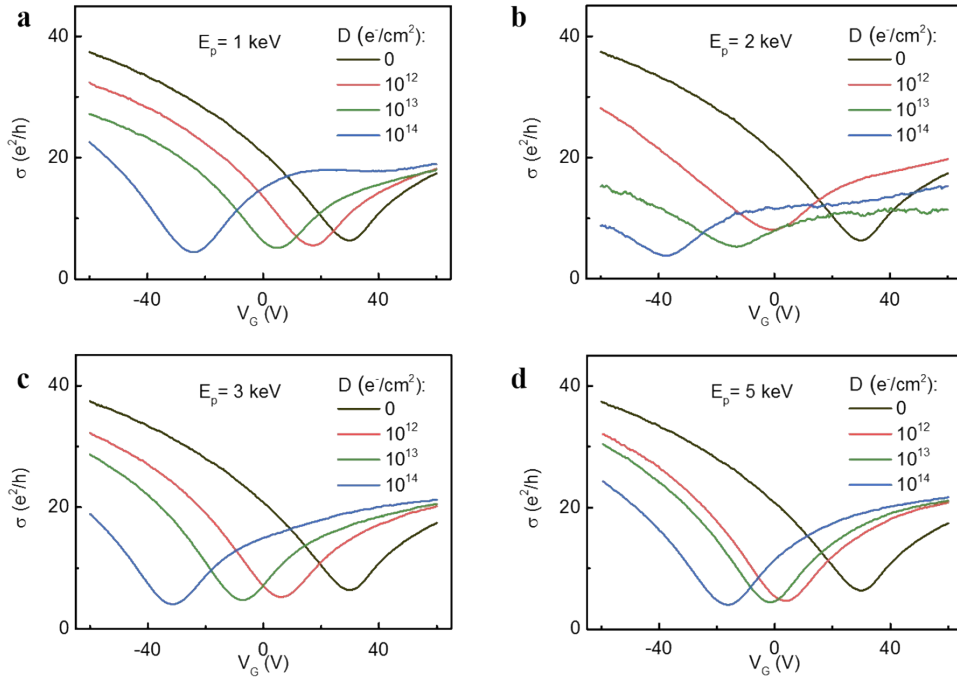


**Fig. S2 Gate responses of graphene FET irradiated by e-beam with different beam energies.** For each beam energy, the gate response were characterized under different doses of  $10^{12} e^-/cm^2$ ,  $10^{13} e^-/cm^2$  and  $10^{14} e^-/cm^2$

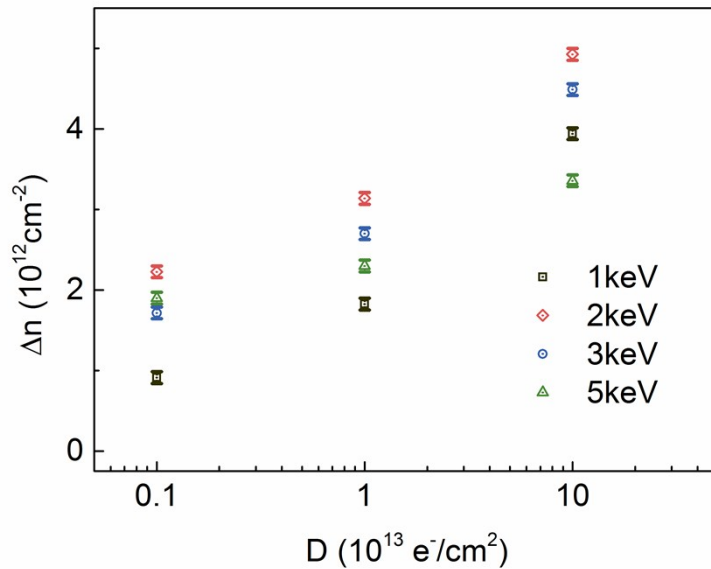


**Fig. S3 The change of electron carrier concentration  $\Delta n$  as a function electron dose for different beam energies of 1 keV, 2 keV, 3 keV and 5 keV.**

## 2. Stability of the e-beam induced n-type doping in vacuum

The stability of the n-type doping in vacuum was investigated by monitoring the evolution of graphene conductivity for a period of 16 hours *in situ* (Fig. S4a) Prior to the e-beam irradiation, the conductivity of pristine graphene was measured at  $\sim 7.3 e^2/h$ , indicating a low carrier concentration around the charge neutrality point. The graphene conductivity exhibited a rapid increase when it was irradiated by a 2 keV beam. A total dose of  $10^{13} e^-/cm^2$  was delivered over a period of  $\sim 2$  s and the beam was then turned off. The doped graphene FET was then left in the scanning electron microscope (SEM) chamber (pressure  $< 2 \times 10^{-5}$  mbar) for 16 hours, and the conductivity gradually increased by  $\sim 20\%$ . The conductivity  $\sigma$  is proportional to the carrier concentration  $n$  and mobility  $\mu$ , i.e.

$$\sigma = ne\mu \quad (\text{S2.1})$$

The change of conductivity ( $\sigma$ ) reflects the change of either the carrier concentration ( $n$ ) or the carrier mobility ( $\mu$ ), or both. Fig. S4b shows the gate response of graphene just after the irradiation and subsequently at the end of the 16 hours, respectively. The Dirac point shifted from  $\sim -38$  V to  $\sim -24$  V, indicating that the carrier density  $\Delta n$  at 0 V back gate decreased by  $\sim 10^{12} cm^{-2}$ , from  $2.8 \times 10^{12} cm^{-2}$  to  $1.8 \times 10^{12} cm^{-2}$ . The gate response of the quenched graphene exhibited a larger slope in the linear response region than that of the just-irradiated, indicating a larger carrier mobility with values increasing from  $\sim 1600 cm^2/V \cdot s$  to  $\sim 2000 cm^2/V \cdot s$ . Therefore, the observed conductivity increase is attributed to the enhancement of carrier mobility, while the doping level only slightly decayed. This shows the n-type doping is stable in vacuum with a decay rate  $\sim 1.9 \times 10^7 cm^{-2} \cdot s^{-1}$ .

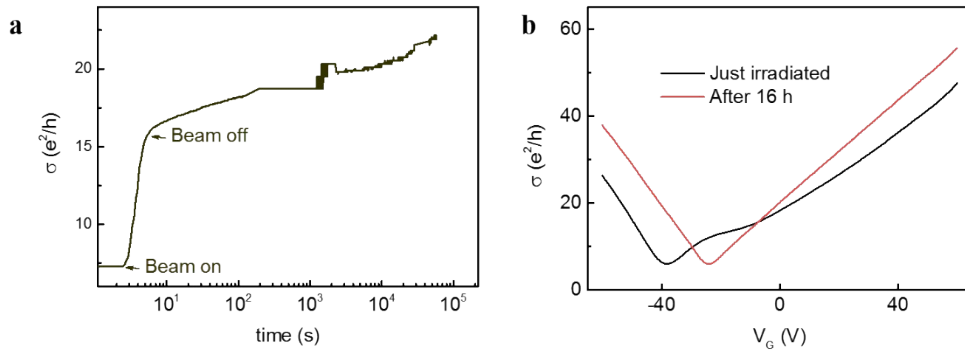


**Fig. S4 Stability of n-type doping.** **a**, Evolution of graphene conductivity after irradiating with a 2 keV e-beam at a dose of  $10^{13} e^- / cm^2$ , and leaving in vacuum for  $\sim 16$  hours. **b**, Gate responses of graphene immediately after irradiation and after 16 hours.

### 3. Erasability of the e-beam induced doping

To show the erasability of the n-type doping, a graphene flake was first heavily n-doped (high conductivity  $> 20 e^2/h$ ) by using a 2 keV beam. After the doping, a beam with a higher energy (10 keV or 20 keV) was used to erase the doping. As shown in Fig. S5, both the 10 keV and 20 keV beams reduced the conductivity to a value close to that of a pristine graphene, indicating the removal of excess electrons in the graphene. The subsequent increase of the conductivity was due to the established p-type doping states (see the doping stability and erasability section in the main manuscript).

The n-type doping of the graphene FET (induced by 2 keV e-beam with  $10^{13} e^- / cm^2$  dose) can be erased by exposing the device to pure nitrogen gas or air. As shown in Fig. S6, the conductivity of the graphene started to increase slightly and then decreased when the system was vented with air. The observed initial rise of conductivity might be attributed to n-type doping caused by the adsorption of thin molecular layers of  $H_2O^1$ , which raises the doping level and thus increases the conductivity. Longer venting time results in more  $H_2O$  molecules adsorbed on the surface, and therefore neutralization of substrate charges and

reduction of the n-type doping level. Doped graphene that is neutralized in nitrogen showed a different trend; the conductivity remained constant after the venting process began, and showed similar behavior (slight increase followed by notable decrease) only after the chamber door was opened to allow exposure to air. The time evolution indicates that  $N_2$  molecules are only physisorbed on the surface and could not neutralize the substrate charges. A gate sweep in air was done after the device was quenched for  $\sim 400$  s, and shows a much larger hysteresis compared to that in vacuum, indicating the adsorption of polar molecules on the graphene surface. The results show that polar molecules such as water can act to erase the doping states by neutralizing the charges within the  $SiO_2$  layer.

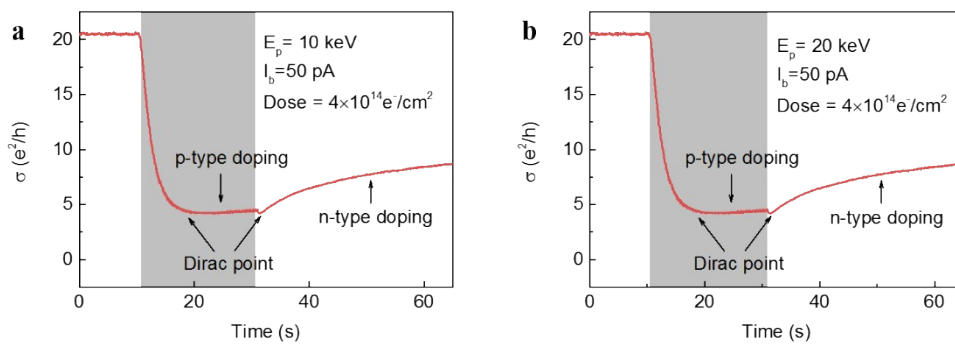


**Fig. S5 Erasing of n-type doping using different beam energies. a**, 10 keV beam irradiation. **b**, 20 keV beam irradiation. The irradiation doses are shown in the figures.

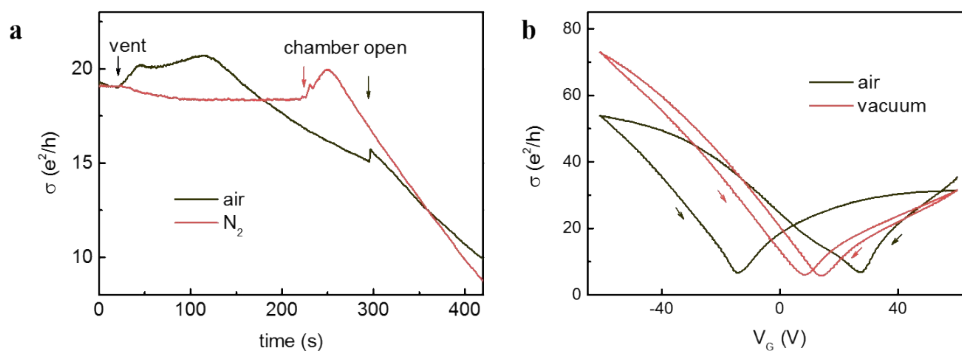


**Fig. S6 Erase of n-type doping by exposing the device in gases. a**, Time evolution of n-type doping in graphene, quenched in nitrogen and air. **b**, Gate sweeps of the irradiated device pre- and post-gas exposure.

#### 4. Evaluation of irradiation induced disorders

The e-beam irradiation can deposit carbon contamination and induce lattice damage to graphene<sup>2, 3</sup>. Here, we evaluate the effect of excessive beam irradiation on graphene quality in view of proposed beam-induced doping and required device functionality. This was done through multiple doping (2 keV beam with a dose of  $10^{14} e^- / cm^2$ ) and erasing (air exposure) cycles. The gate response was characterized before and after each doping stage (Fig. S7). As shown in Fig. S6, the ambipolar behavior of graphene was maintained after a cumulative dose up to  $10^{17} e^- / cm^2$ . At a cumulative dose of  $10^{18} e^- / cm^2$ , the device exhibited strong p-type doping and the Dirac point was out of our back gate sweep range ( $\pm 60 V$ ). The device mobility decreased from  $\sim 2000 cm^2 / V \cdot s$  to  $\sim 5 cm^2 / V \cdot s$  with the increase of the dose (Fig. S8). The shift of the Dirac point  $\Delta V_{Dirac}$  was less prominent when the dose increased, even though the doping process was kept the same for each stage, indicating that effectiveness of the e-beam doping is reduced as the graphene receives more electron dose. From this observation, we comment that the device is re-writable up to  $10^3$  cycles (corresponding to a cumulative dose of  $10^{17} e^- / cm^2$ ). The doping method fails before reaching  $10^4$  cycles.

Raman spectroscopy is also used to investigate the disorders in graphene after irradiating using a large cumulative dose from  $10^{14} e^- / cm^2$  to  $10^{18} e^- / cm^2$ . The results are shown in Fig. S9. The pristine graphene has an ignorable D peak, indicating the high crystal quality with low disorders. The cumulative irradiation dose of  $10^{14} e^- / cm^2$  and  $10^{15} e^- / cm^2$  did not significantly increase the intensity of D peak. However, a higher cumulative dose of  $10^{18} e^- / cm^2$  induced a higher intensity of D peak, indicating more disorders in graphene. The origin of D peak in Raman spectra of e-beam irradiated graphene is in debate. Teweldebrhan et al. attributed the peak to damage and breaking of  $sp^2$  bonds in

graphene<sup>3</sup>. However, a recent study claimed that peak was due to the deposition of amorphous carbon<sup>4</sup>, which does not seem to be plausible as the Raman spectra of amorphous carbons are significant different as the spectra shown in Fig. S9. If the D peak were attributed to the inducing of defects, significant defect scattering behavior would be caused in the electrical transport measurements<sup>5</sup>. In addition, this effect is irreversible. In our experiments, the conductivity of irradiated device slightly reduced after irradiation and could be recovered to its initial states after being exposed in air. This results are contradict with the defect scattering phenomenon but could be well explained by the charged impurity scattering theory. Therefore, in our results, the Raman D peak could not be simply attributed to defects. A plausible explanation to the appearance of the D peak may be the disorder effect<sup>6</sup>. These results are also consistent with the electrical properties of graphene shown in Fig. S7, which graphene receives low damage and maintains its intrinsic properties under low irradiation doses ( $\sim 10^{16} e^- / cm^2$ ) but gets damaged under high irradiation doses ( $\sim 10^{18} e^- / cm^2$ ).

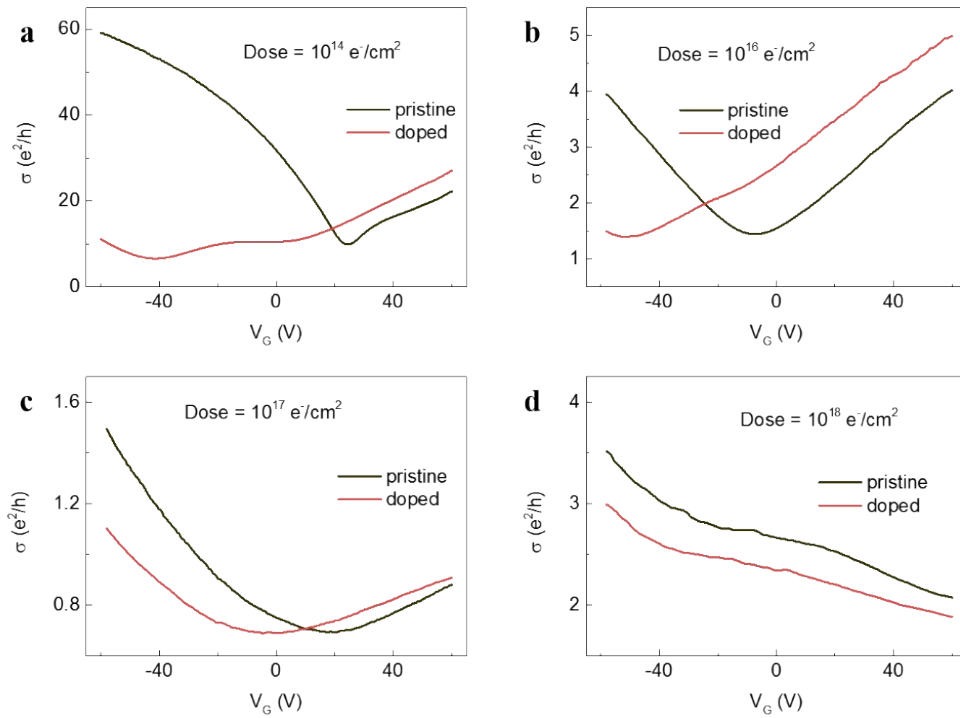


**Fig. S7 N-type doping behavior of graphene under different irradiation doses.** Note that the data point for the dose of  $10^{15} e^-/cm^2$ , which includes the carrier concentration and mobility, was extracted from a different flake.

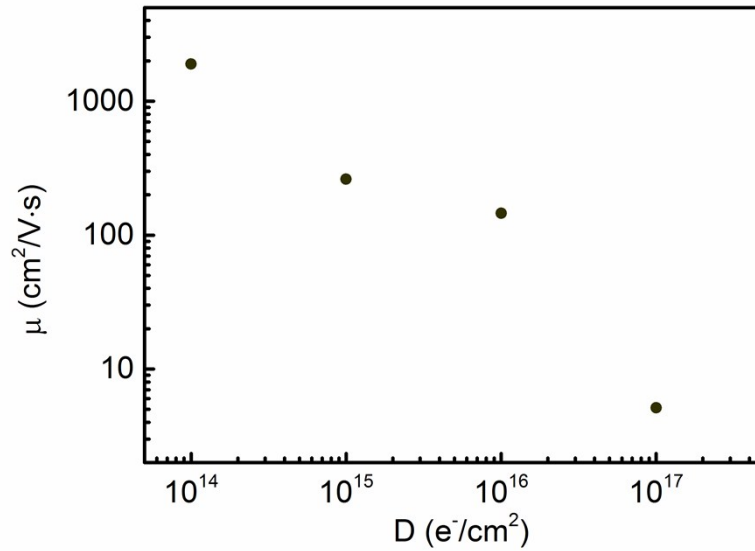


**Fig. S8 Decrease of electron mobility at different irradiation doses.**

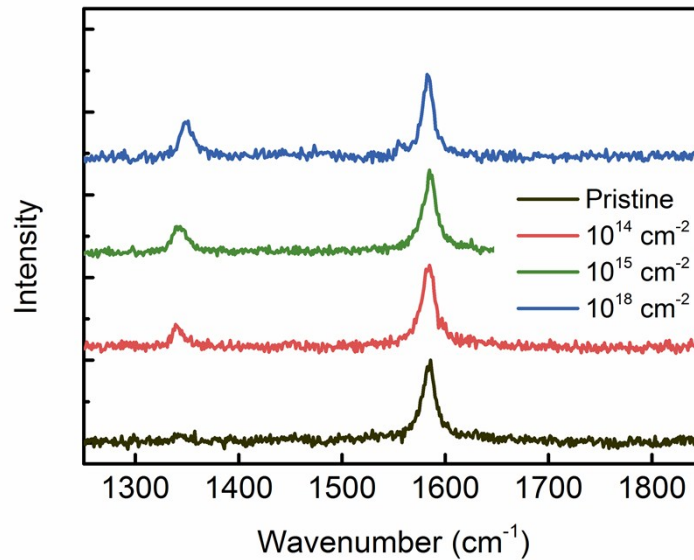


**Fig. S9 Raman spectra of graphene under high cumulative dose.** The beam energy is 2keV.

## 5. The physical model of beam induced graphene doping

Here we develop the physical model for the e-beam induced doping in graphene. A focused e-beam of energy  $E_p$  (ranging from 1 keV to 30 keV), is used to irradiate a graphene FET device on a SiO<sub>2</sub>/Si substrate ( $d_{\text{SiO}_2} = 285$  nm) with a dose  $D$  (number of incident electrons per unit area), which also cause charging of the supporting substrate. Net negative charges may accumulate within the substrate due to the injection of primary electrons, with additional contributions from back-scattered electrons (BSEs) and secondary electrons (SEs). The step size ( $\sim 20$  nm) and probe size ( $> 20$  nm by defocusing the beam) are adjusted to deliver a uniform dose across the irradiated region. The dose variance is dominated by the stability of beam current, and we observed an uncertainty of  $\sim 1$  pA for the 20 pA e-beam, which corresponds to a dose variation of  $< 5\%$ . The irradiated area ( $\sim 30 \times 30 \mu\text{m}^2$ ) is much larger than the graphene flake size ( $< 10 \times 10 \mu\text{m}^2$ , located at the center of irradiated area) and the boundary effect is negligible. Therefore, we assume the charges are uniformly distributed under the graphene and the charge distribution in the substrate is symmetric radially from the axis of the incident beam on the substrate. The effective charge area density ( $n_{\text{sub}}$ ) is determined by the primary electron dose ( $D$ ), the BSE yield ( $\eta$ ) and the SE yield ( $\delta$ ):

$$n_{\text{sub}} = n^+ + n^- = (\sigma - 1)De \quad (\text{S5.1})$$

where  $n^- = -(1 - \eta)De$  is the concentration of injected negative charges taking into account escaped BSEs,  $n^+ = \delta De$  is the concentration of the irradiation-induced positive charges in the substrate due to the escape of SEs, and  $\sigma = \delta + \eta$  is the total electron emission yield. Here we only consider the SE emission from SiO<sub>2</sub> substrate, since the SE yield of graphene itself is quite low comparing with SiO<sub>2</sub> substrate and can be ignored<sup>7</sup>. These additional charges will generate an electric field. This field is equivalent to one that would be produced by a back gate. Concomitantly, charges will accumulate in graphene to screen this electric field, which changes the carrier density in the graphene. Due to the weak interaction between graphene

and SiO<sub>2</sub> substrate, the interaction effect could be ignored<sup>8</sup>. If we assume a perfect screening, the carrier concentration in graphene is thus

$$n_{gra} = -n_{sub} = -(\sigma - 1)De \quad (S5.2)$$

The carrier concentrations in the graphene is determined by the density of the excess charges ( $n_{sub}$ ) in the underlying substrate induced by the e-beam irradiation. The calculation of  $n_{sub}$  is carried out through an iteration process, since the accumulation of the excess charges in the substrate modifies the subsequent SE emission, which in turn changes the accumulation of the excess charges. We first evaluate the charge density of the injected primary electrons followed by the derivation of the near surface charging effect.

During the beam irradiation, the injected primary electrons modify the charge density in the substrate. The injected electron density can be calculated by using Casino software (v 2.4)<sup>9</sup>, as shown in Fig. S10. For the 2 keV beam with a dose of  $10^{13} e^- / cm^2$ , all the injected electrons stay in the range of 10-120 nm, which are within the insulating SiO<sub>2</sub> layer (Fig. S10a). The overall areal density of the injected electrons is  $8.7 \times 10^{12} cm^{-2}$ , which is 10% smaller than the irradiation dose because of the back scattering effect. The density of the injected electrons as a function of the injection depth is fitted with a Gaussian profile and written as:

$$n^-(t) \cong \exp\left[-\frac{1}{2}\left(\frac{z/nm - 60.3}{23.2}\right)^2\right] \times 3.08 \times 10^{12} cm^{-2}$$

This profile is used for the evaluation of the built-in potential and the SE emission.

We then evaluate the substrate surface charging due to SE emission. At time  $t$ , we assume the SE yield is  $\delta(t)$  for an accumulated irradiation dose  $D(t)$ , and the excess charge density  $n_{sub}(t)$  is given by

$$n_{sub}(t) = n^+(t) + n^-(t) = -(\delta(t) + \eta - 1)D(t)e \quad (S5.3)$$

These charges can be regarded as uniformly distributed in the x-y plane, which is parallel to the surface, therefore we only need to consider its distribution in z direction. The potential induced by charges can be described by the Poisson Equation

$$\frac{d^2 U(z,t)}{d^2 z} = - \frac{\rho(z,t)}{\epsilon_0 \epsilon_r} \quad (\text{S5.4})$$

Where  $\rho(z,t)$  is the charge density at a given depth  $z$  and time  $t$ , and  $\epsilon_r = 3.8$  is the dielectric constant of SiO<sub>2</sub>. It is given by the piecewise function:

$$\rho(z,t) = \begin{cases} n_{gra}(t) & z = 0 \\ \rho^+(z,t) + \rho^-(z,t) & 0 < z \leq d \\ \rho^-(z,t) & z > d \end{cases} \quad (\text{S5.5})$$

Where  $d$  is the SE escape depth, where the positive charges are generated and is typically 10 nm.

We make several assumptions to simplify Equations (S5.4) and (S5.5). Firstly, we assume the

positive charges are uniformly distributed along the depth  $d$ , i.e.  $\rho^+(z,t) = \frac{n^+(t)}{d(t)}$ , for  $0 < z \leq d$ . Secondly, for the discussed 2 keV beam irradiation, the electron range extends from  $z = 10 \text{ nm}$  to  $180 \text{ nm}$ , therefore its distribution within the SE escaped depth can be ignored ( $< 0.3\%$ ),  $\rho^-(z,t) = 0$ , for  $0 < z \leq d$ . The potential distribution  $U(z,t)$  at  $0 < z \leq d$  is important because it affects the SE escaping process. The initial boundary condition is determined by connecting the graphene surface to ground, and is hence  $U(0,t) = 0$ . The solution to equation (S5.4) is then given by:

$$U(z,t) = \frac{(n^-(t) + \frac{n^+(t)}{2}) \cdot d}{\epsilon_0 \epsilon_r}$$

(S5.6)

The potential difference across the SE escaping region is thus given by:  $\Delta U(t) = U(d,t)$ . The escape depth  $d$  is also affected by the charges and built-in electric field:

$$d(t) = d_0 \cdot e^{-\frac{\overline{E}(t)}{E_a}} \quad (\text{S5.7})$$

where  $d_0 \approx 10 \text{ nm}$  is the escape depth for SEs within  $\text{SiO}_2$  layer with no electricfield, and is a constant<sup>10</sup>.  $\overline{E}(t)$  is the mean electric field in the SE escaping region

$$\overline{E}(t) = \frac{\Delta U(t)}{d} = \frac{(n^-(t) + \frac{n^+(t)}{2})}{\epsilon_0 \epsilon_r} .$$

The potential will decelerate SEs while penetrating to

surface, allowing us to write the SE emission yield as<sup>11</sup>

$$\delta(t) \propto \int_{e\Delta U(t)}^{50 \text{ eV}} \frac{E_K}{(E_K + \chi)^3} dE_K \quad (\text{S5.8})$$

where  $\chi = 0.9 \text{ eV}$  is the electron affinity for  $\text{SiO}_2$ . We can integrate S5.8 and get

$$\delta(t) = \delta_0 \cdot \frac{\frac{2\Delta U(t)}{\chi} + 1}{(\frac{\Delta U(t)}{\chi} + 1)^2} \quad (\text{S5.9})$$

where  $\delta_0 \propto \int_0^{50 \text{ eV}} \frac{E_K}{(E_K + \chi)^3} dE_K$  is the SE yield without the built-in field. During the irradiation, for an interval  $\Delta t$ , an additional dose of  $\Delta D$  is delivered, the delivered dose becomes  $D(t + \Delta t) = D(t) + \Delta D$ . From equations (S6.1) to (S6.5) we can then use  $\delta(t)$ ,  $U(t)$ , and  $D(t + \Delta t)$  to evaluate the excess charge density  $n_{sub}(t + \Delta t)$ . For 2 keV irradiation presented in the inset of Fig. 1c, we used BSE yield  $\eta = 0.13$  acquired from a Casino simulation (see section 7) and  $\delta_0 = 1.65, 7$ . The dose increases from 0 to  $10^{14} \text{ e}^- / \text{cm}^2$  with a constant step size of  $10^{11} \text{ e}^- / \text{cm}^2$ , the result is shown as the dashed line in inset of Fig. 1c. The variation of doping level at saturation between devices can be explained by the difference in quality of the oxide layer between different chips, thus affecting the SE emission yield. To verify this, we

used different values of  $\delta_0$  to fit the change of doping concentrations  $\Delta n$  for six different samples shown in Fig. S1. The lowest  $\Delta n$  of  $4 \times 10^{12} \text{cm}^{-2}$  can be fitted using  $\delta_0 = 1.6$  (dashed line in Fig. S11(a)), while the highest  $\Delta n$  of  $5 \times 10^{12} \text{cm}^{-2}$  can be fitted using  $\delta_0 = 1.9$ . The results show that a 20% variation of SE yield without the built-in field, which increases from 1.6 to 1.9, corresponds to the change of carrier concentration  $\Delta n$  from  $4 \times 10^{12} \text{cm}^{-2}$  to  $5 \times 10^{12} \text{cm}^{-2}$ . Besides the SE yield, electron affinity of  $\text{SiO}_2$  will also affect e-beam induced doping. We also calculated the doping behavior using different values of electron affinity at same SE yield of 1.6 (Fig. S11(b)). The results show the same saturation behavior of e-beam induced doping. The most significant difference is the doping saturation level.

The variation of saturated doping levels shown in Figs. S2 and S3 can also be understood as the change of surface potential. The SE yield has been verified to be reduced as the beam energy increases from 1 keV to 5 keV. Equation (S5.6) can be applied to explain the doping behavior for beam energies higher than 2 keV, where the doping levels are reduced as the beam energy increases due to the decrease of SE yield  $\delta_0$ . For lower beam energies (e.g. 1keV shown in Fig. S2), part of the injected electrons stays in the SE escape region; their contribution to the electric field (The fourth term in equation S5.4) needs to be considered. The actual field strength will be larger than calculated, thus creating a larger surface potential. It will correspond to a faster decrease of SE yield thus a lower saturation value of the doping level.

For beam energies higher than 5 keV, the penetration depth of electrons is larger than 300 nm and some of the injected electrons penetrate the  $\text{SiO}_2$  layer and reach the Si substrate (Figs. 10b and 10c). The higher the primary beam energy, the less injected electrons are left in the  $\text{SiO}_2$  layer. At a beam energy of 30 keV, almost all electrons (> 99.9 %) are embedded deeply into Si substrate with a range of 1  $\mu\text{m}$  to 10  $\mu\text{m}$  (Fig. S10d). The charges remaining in

the SiO<sub>2</sub> layer are negligible. Meanwhile, the SE yield is inversely proportional to the high beam energies. For example, the yield is less than 0.5 for beam energies higher than 10 keV<sup>10</sup>. The low SE yield results in low densities of surface charges and p-type doping in graphene. Equation S5.6 can still be applied to describe the establishing of the surface potential and its influence on the SE escaping process. However, since the electrons are injected into Si substrates and can have a larger diffusion rate due to the higher mobility in Si than in SiO<sub>2</sub>.  $n^-(t)$  is expected to decrease as the time  $t$  increases. The p-type doping level will then also decrease as the time increases.

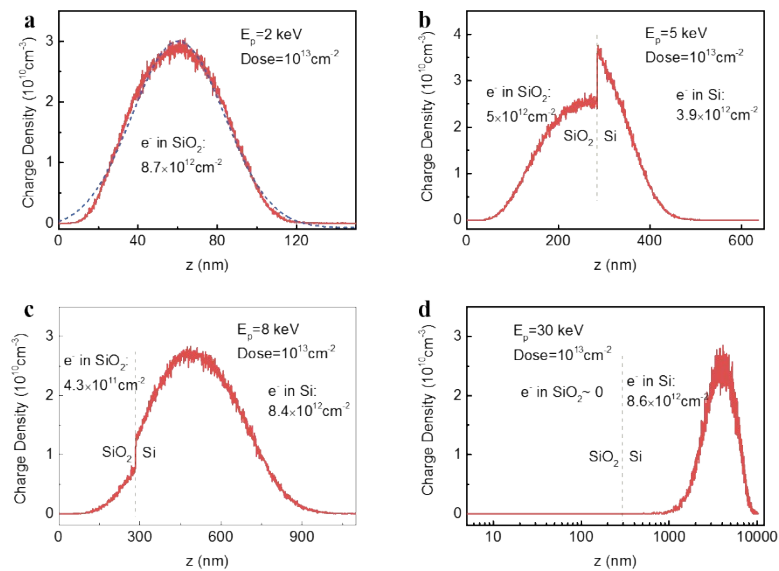


**Fig. S10 Simulations of charge distribution of electrons with different energies.** The blue short-dashed line in **a** shows the fitting using Gaussian distribution.

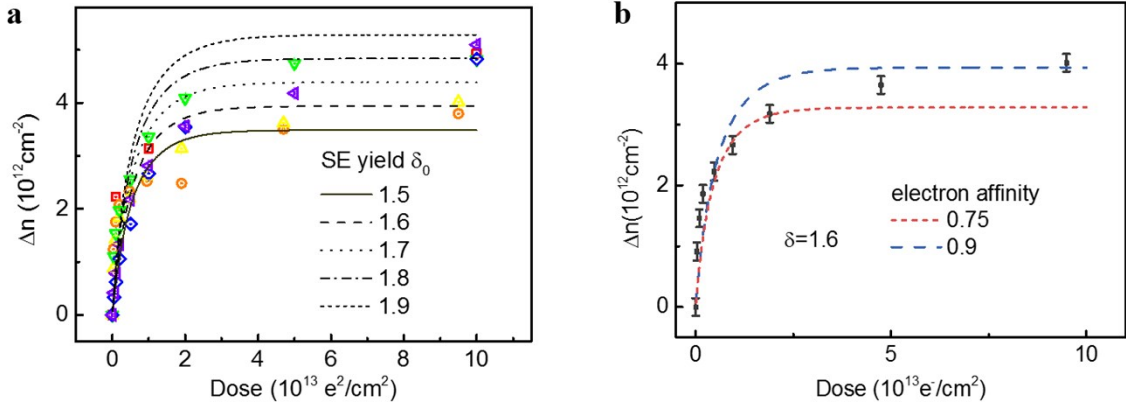


**Fig. S11 Calculated influence of SE yield and electron affinity of SiO<sub>2</sub> to induced doping.**

(a) Fitting of  $\Delta n$  for six different samples in Fig. S1. The values of  $\delta_0$  use for fitting range from 1.6 to 1.9. (b) Calculated doping behaviors using two different values of electron affinity.

## 6. Impurity scattering in graphene

According to Matthiessen's Rule, the conductivity of graphene has contributions from various possible scattering sources<sup>12</sup>:

$$\sigma^{-1} = \sigma_{ci}^{-1} + \sigma_{sr}^{-1} + \sigma_{mg}^{-1} + \sigma_{LA}^{-1} + \sigma_{PO}^{-1} + \sigma_{corr}^{-1} \quad (S6.1)$$

where the subscripts indicate the contributions from charged impurities (ci), short-range scatterers (sr), mid-gap states (mg), longitudinal acoustic phonons (LA), polar optical phonons (PO) and surface corrugations (corr) respectively. Previous reports show that for the diffusive region with moderate carrier density (typically orders of  $10^{12} \text{ cm}^{-2}$ ) the dominant process is the charged impurity scattering, which gives rise to a conductivity linear in carrier density, i.e.

$$\sigma_{ci}(n) = C_{ci} e \left| \frac{n}{n_{imp}} \right| \quad (S6.2).$$

where  $C_{ci} = 5 \times 10^{15} \text{ V}^{-1} \text{ s}^{-1}$  is a constant for impurities with a distance  $\sim 1 \text{ nm}$  away from graphene<sup>9</sup>,  $n_{imp}$  is the impurity density. The linearity is also observed in our experiments (see

Fig. 1c and Fig. S12, the sublinear behavior at higher carrier densities is due to the existence of short-range scatterers), so we assume the charged impurity is the dominant scattering mechanism in our sample.

The carrier density dependence of graphene conductivity can be written as:

$$\sigma^{-1}(n) = (ne\mu)^{-1} + \sigma_{res}^{-1} \quad (S6.3)$$

where  $\mu$  is the mobility mediated by charged impurity scattering. Equation (S6.3) is used to fit the gate response curves of graphene, such as those shown in Fig. 1c. The fitting to pristine graphene shows the electron and hole mobilities are  $\sim 1.06 \times 10^4 \text{ cm}^2/\text{V} \cdot \text{s}$  and  $8.9 \times 10^3 \text{ cm}^2/\text{V} \cdot \text{s}$  respectively (Fig. S12). By combining Eqs. (S9.2) and (S9.3) we obtain the relationship between mobility and charged impurity density:

$$\frac{1}{\mu} = \frac{n_{imp}}{C_{ci}} = \frac{n_{imp}}{5 \times 10^{15}} (\text{V} \cdot \text{s}) \quad (S6.4)$$

In our experiment, the impurities correspond to positive charges generated by SE emission and distributed close to the surface within a depth  $d_0 \approx 10 \text{ nm}$  i.e.  $n_{imp} \propto n_+ = D \cdot \delta$  (see section 5 on the discussion of SE emission and surface charging). The effects of injected electrons can be ignored since less than 0.03% of them stay in this surface layer ( $\sim 10 \text{ nm}$ ). This means that the mobility is inversely proportional to the dose. The inset of Fig. 3c (reproduced here as Fig. S13) shows that the carrier mobility is inversely proportional to the dose, corroborating the model of beam-induced charged impurity. The relationship fails at high doses ( $>10^{13} \text{ e}^-/\text{cm}^2$ ). This is due to the failure of the linear dependence of surface charging on the beam dose ( $n_+ = D \cdot \delta$ ), since SE yield was suppressed by the surface charge. Nevertheless, with a SE yield  $\delta=1.6$  for the 2 keV beam, in the linear region of Fig. S13, the electron mobility ( $\mu_e$ ) and surface positive charge density ( $n_+$ ) can be written as:

$$\frac{1}{\mu_e} \cong \frac{n_+}{(3.9 \pm 0.3) \times 10^{17} (V \cdot s)} \quad (S6.5)$$

This establishes a quantitative relationship between the density of charged impurities responsible for the carrier scattering in graphene and the surface positive charge due to SE emission, i.e. from Equations S6.4 and S6.5, we have

$$n_{imp} = 0.013n_+ \quad (S6.6)$$

Those closest to the graphene dominate the charged-impurity scattering behavior in the device. The fitting parameter indicates that  $\sim 1\%$  of positive charges contribute to the scattering. This roughly corresponds to positive charges in the top  $<1$  nm of the oxide rather than the entire  $\sim 10$  nm region that is depleted of electrons by beam-induced SE emission.

The minimal conductivity ( $\sigma_{min}$ ) at the charge neutrality point is dominated by the residual carrier density ( $n_{res}$ ) due to the electron-hole puddle effect caused by charged impurities<sup>13</sup>. The residual carrier density can be evaluated from the plateau width of minimal conductivity ( $\Delta V_g$ ), which we estimated from the distance between two fitted mobility curves on the electron and hole doping branches of the curve (see Fig. S12).  $n_{res}$  is given by:  $n_{res} = \alpha \cdot \Delta V_g$ , where  $\alpha = 7.3 \times 10^{10} cm^{-2} V^{-1}$  is a constant. Fig S14b shows the evolution of minimal conductivity under the 2 keV e-beam irradiation. The minimal conductivity of the pristine graphene is  $\sim 9.5e^2/h$ , which corresponds to an initial charge impurity of  $\sim 3 \times 10^{11} cm^{-2}$ . The impurity density is at a lower level compared to previous reports<sup>13</sup>, indicating that the surface of the pristine graphene is clean. The e-beam irradiation reduces the minimal conductivity which approaches a value of  $\sim 6e^2/h$  at high doses ( $\sim 10^{14} e^- / cm^2$ ).

Taking into account the deterioration of the carrier mobility, we estimate the residual charge concentration  $n_{res}$  as a function of the dose, which is shown in Fig. S14c. The residual charge concentration increases with dose. This is clear evidence that the near-surface charge

impurities introduce a fluctuation of the Coulomb potential, which results in the electron-puddle effect.

The scattering behavior caused by 30 keV e-beam irradiation is shown in Fig. S15. The mobility exhibits similar decaying behavior as in the case of 2 keV beam irradiation (Fig. S15a and Fig. 3c). However, the mobility is higher at the same dose. This is consistent with the surface charging model where the high energy e-beam returns a lower SE yield, thus a smaller positive charge density and less scattering. The minimal conductivity also reduces as the dose is increased (Fig. S15b). However, the extracted residual carrier density increases after irradiation and then maintains a constant value of around  $4.5 \times 10^{11} \text{cm}^{-2}$  (Fig. S15c). The density is less than for the 2 keV irradiation at the same dose, which indicates less scattering events and leads to higher mobility.

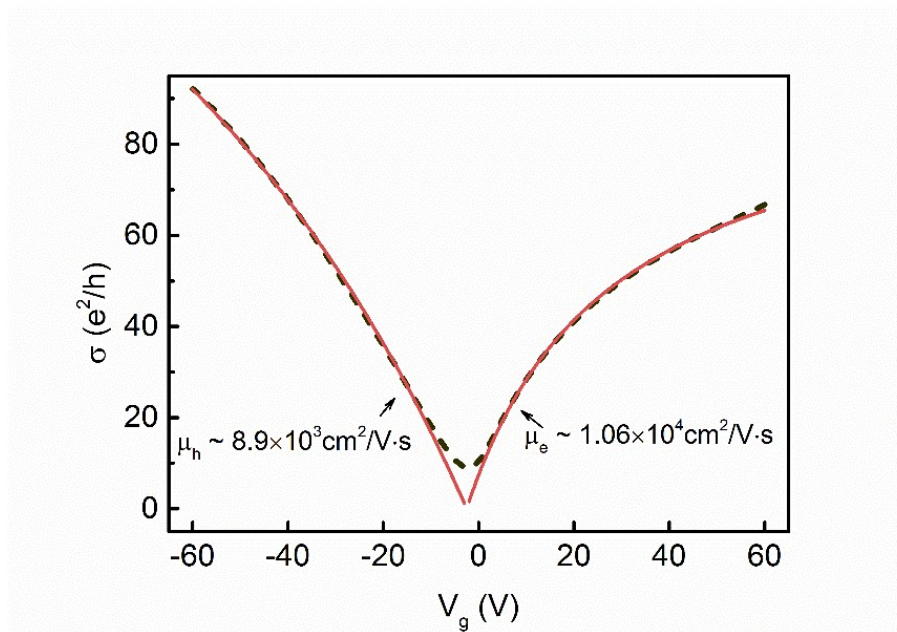


**Fig. S12 Fitting of the pristine graphene gate response curve using Equation (S9.3)**

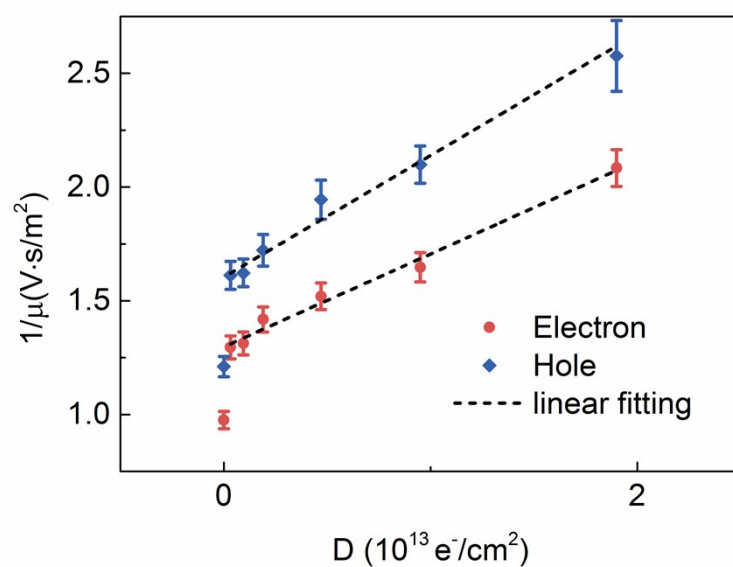


**Fig. S13 inverse mobility as a function of e-beam dose with linear fitting.**

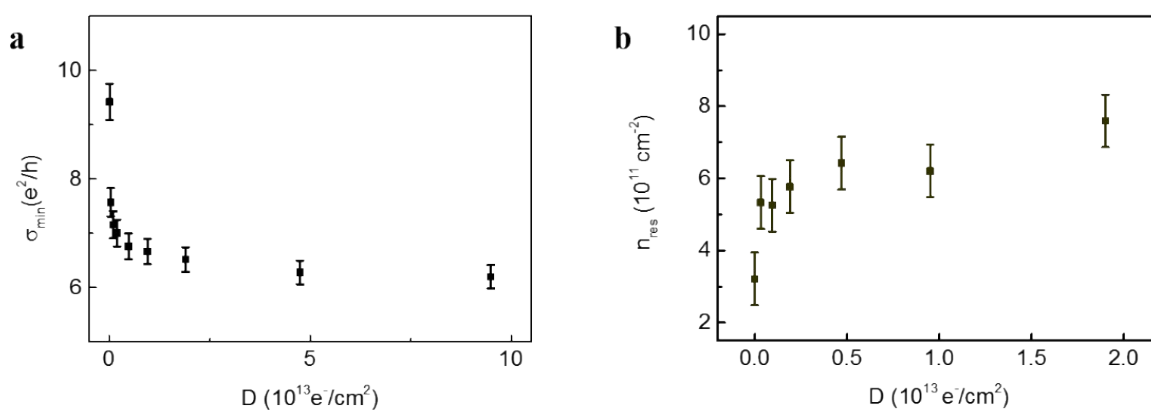


**Fig. S14 Charged impurity scattering behavior in graphene caused by 2 keV beam irradiation. a,** minimal conductivity as a function of electron dose. **b,** residual carrier density as a function of electron dose.

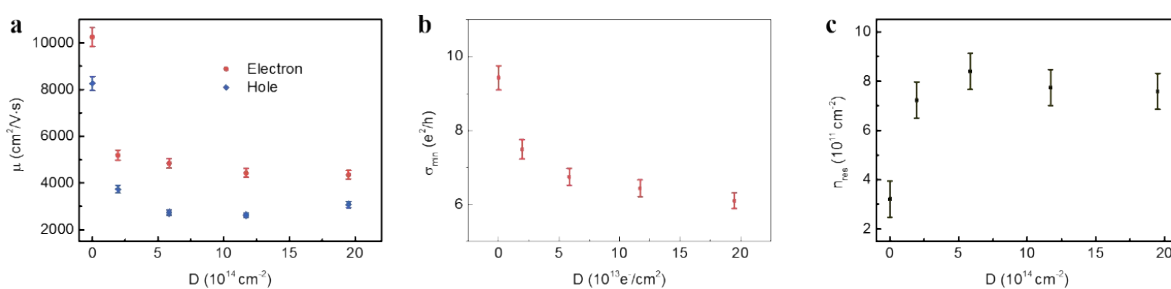


**Fig. S15 Charged impurity scattering behavior in graphene caused by 30 keV beam irradiation. a,** electron and hole carrier mobility as a function of electron dose. **b,** minimal conductivity as a function of electron dose. **c,** residual carrier density as a function of electron dose.

## 7. Comparison with previous reports

We compare our results with previous reports, as shown in table S1, these results usually used e-beams with high energies (20-30 keV) and large doses (from  $10^{16} e^- / cm^2$  to  $10^{17} e^- / cm^2$ ) to obtain n-type doping with doping level no higher than  $2 \times 10^{12} cm^{-2}$ . Most of these experiments were carried out ex situ, i.e. devices taken out of SEM chamber first before following measurements, which may be in vacuum as well. The issues that limit doping level is not discussed. While in our results, we used low energy e-beams (2 keV) with irradiation doses of 2-3 orders of magnitude lower ( $< 10^{14} e^- / cm^2$ ) to obtain a higher n-type level ( $4.5 \times 10^{12} cm^{-2}$ ). Although our p-type doping is unstable, the irradiation dose is still 1-2 orders lower, while the maximum doping level is at the same order. Note that ref 18 did similar in-situ measurements as ours, and obtained the similar doping level as well. However they used large irradiation dose. And they attributed this doping effect to electrons trapped in the SiO<sub>2</sub> layer during irradiation, which seems wrong as it will cause p-type doping instead.

Reference	Beam energy (keV)	Dose ( $e^- / cm^2$ )	Doping type	Doping level ( $cm^{-2}$ )	Measurement environment
Childres et al. Appl. Phys. Lett., 2010, 97, 173109. (Ref 18) <sup>14</sup>	30	$4.5 \times 10^{17}$	n-type	$\sim 1.5 \times 10^{12}$	Ex situ
Liu et al. IEEE Transactions on Nanotechnology, 2011, 10, 865-870. (Ref 19) <sup>15</sup>	20	$8 \times 10^{15}$	n-type	$\sim 10^{12}$	Ex situ
Hossain et al. Appl. Phys. Lett., 2013, 102, 153512. <sup>16</sup>	20	$6 \times 10^{16}$	n-type	$\sim 5 \times 10^{11}$	Ex situ
Iqbal et al. Carbon, 2013, 59, 366-371. <sup>17</sup>	20	$7.5 \times 10^{16}$	n-type	$\sim 2 \times 10^{12}$	Ex situ

Yu et al. Sci. Rep., 2015, 5, 12014. <sup>18</sup>	20	$1.2 \times 10^{16}$	n-type	$\sim 1.5 \times 10^{12}$	Ex situ
Y. H. He et al. Appl. Phys. Lett., 2011, 99, 033109. <sup>19</sup>	10	$8.1 \times 10^{16}$	n-type	$\sim 5 \times 10^{12}$	In-situ
Our results	2	$10^{14}$	n-type	$\sim 4.5 \times 10^{12}$	In-situ
Our results	30	$10^{15}$	p-type	$\sim 10^{12}$ (unstable)	In-situ

Table R1 Comparison of our results and previous reports

## 8. NOT gate operation (graphene inverter)

Fig. S16a shows the gate transfer curves for the entire device (yellow curve), the undoped region A (red curve) and the doped region B (purple curve). The gate response of the total device shows two separated minima. The contribution to these two minima can be verified by varying the irradiation doses while monitoring their positions (Fig. S18b). The minimum on the right-hand side has the same location for different doses, which corresponds to the response from the undoped region A. The left-hand side minimum consistently shifts to lower gate voltages as the dose is increased, demonstrating the increased level of the doping acquired by region B of the device. Therefore, these two minima represent the deconvoluted contributions to the total device signal. The output voltages can also be tuned while varying the irradiation doses (Fig. S18c). After the selective irradiation at the dose of  $10^{12} e^- / cm^2$ , the logic inverter exhibits a clear magnitude drop (over 20 %) in the output voltage signal across the 20 V to 0 V back gate bias region (orange curve). When the e-beam doses increase to  $10^{13} e^- / cm^2$  (blue curve) and  $10^{14} e^- / cm^2$  (red curve), the back gate bias separation between the high and low output states increases, as does the  $V_{out}$  read-out ratio between them. This inverse logic output can be reset by erasing the selective doping profile. The exposure of the whole device to the e-beam at an energy of 30 kV with dose of  $10^{15} e^- / cm^2$  will initialize the device to a constant output (green line in Figs. 16c).

To quantitatively evaluate the logic output performance, we calculate the change of high/low output ratio and device gain with electron beam dose, as illustrated in Fig. S17. We

note the significant deterioration of the ratio for irradiations of region B at 30 kV (Fig. S17a), demonstrating the ability to reverse the functionality of the device by choice of appropriate beam energy. Fig. S17b shows the different gains of the inverter under different doping levels. The lowest doping level ( $10^{12} e^- / cm^2$ ) has the largest gain ( $\sim 0.02$ ) while the gain reduces to  $\sim 0.014$  at higher doping levels. Although the high and low  $V_{out}$  signals are clearly distinguishable for the case of n-type doping with different doses of the 2 keV electron beam, the gain value is quite low. Future research strategies may wish to address this issue by changing the thickness of the gate oxide or using a top gate to improve the sensitivity of  $V_{OUT}$  to changes in applied  $V_{IN}$ .

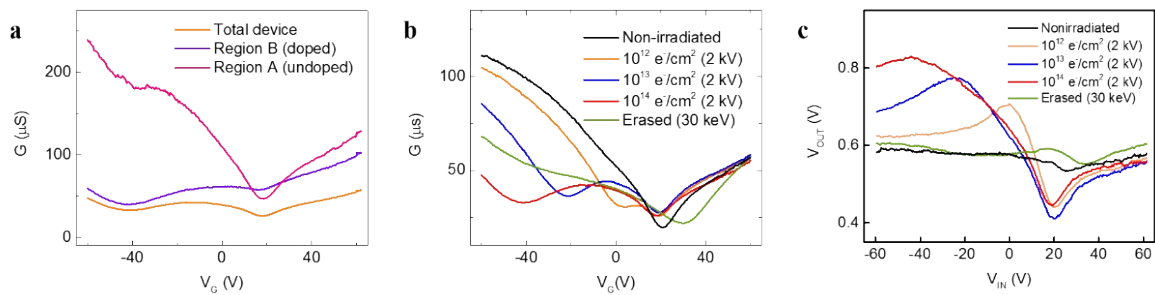


**Fig. S16 Tunability of graphene inverter.** **a**, gate responses for doped and un-doped regions in a monolayer graphene inverter, and the entire device containing these two regions connected in parallel. **b**, gate response of graphene inverter with region B irradiated by a 2 keV beam with different doses, followed by the irradiation using a 30 keV beam with a dose of  $10^{15} e^- / cm^2$ . **c**, output voltage response of graphene inverter with the e-beam irradiation conditions mentioned in **b**.

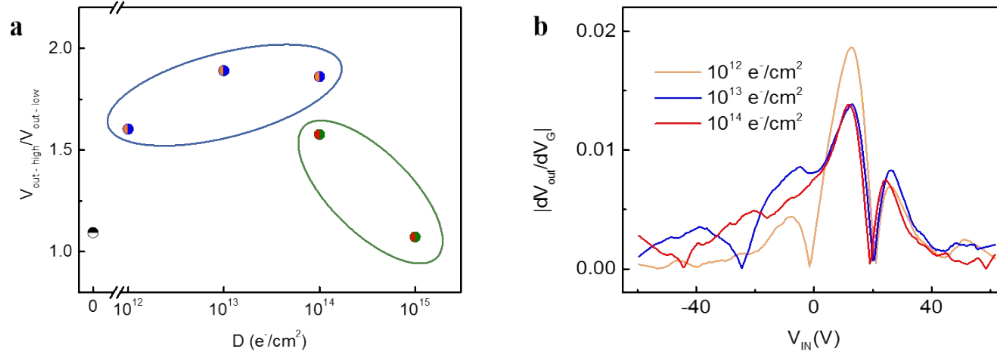


**Fig. S17 Gain of the inverter under different doping levels. a,** the change of high/low output ratio as a function of electron dose. **b,** device gain as a function of electron dose.

## 9. Fabrication of programmable logic device.

Fig. S18 shows the fabrication process for the tested programmable logic device. First, graphene flakes were mechanically exfoliated on a  $SiO_2/Si$  substrate. Graphene flakes with size larger than  $10 \mu m \times 8 \mu m$  were selected for the following fabrication process (Fig. S18a). The graphene was first plasma etched to the designed shape using PMMA resist as a mask, followed by standard EBL processing and metal film deposition Ti/Au (5 nm/35 nm respectively) to make electrodes (Fig. S18b). Boron nitride flakes (SPI Supplies) were mechanically exfoliated on another  $SiO_2/Si$  substrate. Flakes of green color (as shown in the figures) were selected for the experiment and polymer stamp-transferred on top of the graphene device as an insulating layer (Fig. S18c). The layer thickness was later determined to be  $\sim 23$  nm by atomic force microscopy. Finally, an additional EBL process followed to deposit electrodes (50 nm Au) on top of the BN layer as top gate inputs (Fig. S18d). Before the experiment, the two input gates were tested independently by applying a gate bias to check their leakage currents. Our experiments show that for this 23 nm BN flake, the applied voltage of up to 4 V does not cause the electrical breakdown of the insulating layer.

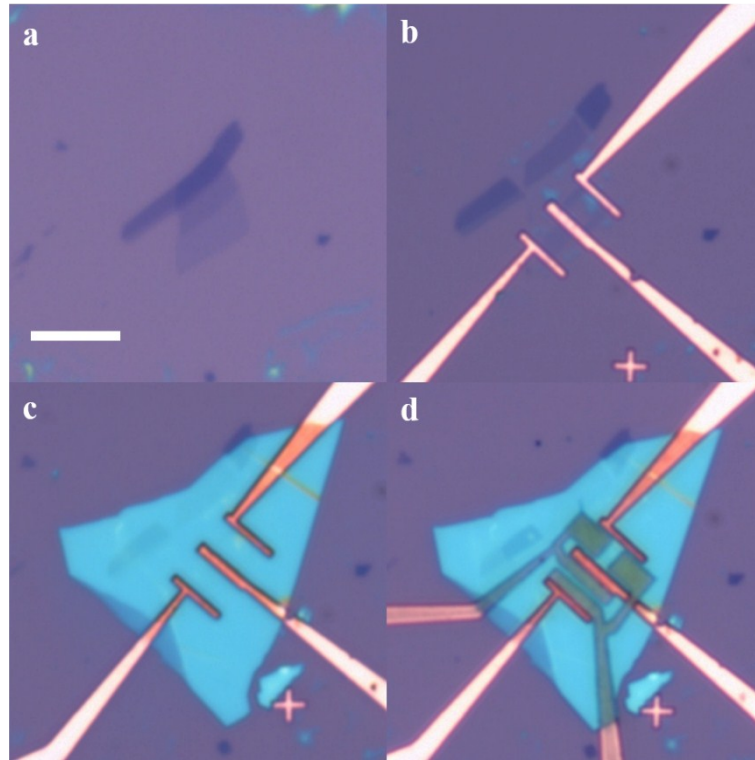


**Fig. S18 Optical images showing the fabrication process of graphene programmable logic devices.** **a**, Suitable mechanically exfoliated graphene flake is chosen under the optical microscope. **b**, Following plasma-etching, EBL-deposited electrodes are introduced. **c**, A boron-nitride flake is transferred onto the graphene device through a site-specific polymer stamp transfer process using micro-manipulators. **d**, A top gate is patterned on top of the BN in a subsequent EBL step. The scale bar is 10  $\mu\text{m}$ .

#### 10. Electron beam-induced doping of other 2D materials.

Fig. S19a shows the determination of the threshold voltage from a gate curve of pristine mechanically-exfoliated  $\text{MoS}_2$ . The figure is plotted on a linear scale rather than a semi-log scale. A linear region is observed for positive gate bias from +40 V to +60 V. We performed a linear fit for this region, extrapolating the fitted line to the abscissa ( $\sigma = 0$ ), where the intercept is defined as the threshold voltage. Fig. S19b shows the conductance change for a monolayer  $\text{MoS}_2$  at 0 V back gate. The device has a low conductance before irradiation,

which can be regarded as an insulating “OFF” state. After being irradiated by a 2 keV beam, the conductance increases. The  $10^{14} e^-/cm^2$  dose of irradiation causes the increase of conductance over two orders of magnitude, demonstrating a conductive “ON” state. We extracted the field effect mobility of doped MoS<sub>2</sub> at approximately the same carrier concentration, which was done at the positions of the threshold voltage and 10 V away from the threshold voltage. At both positions, the mobility increases as the electron dose increases (Fig. S19c). The results differ from the behavior of doped graphene, and suggest that more scattering mechanisms may need to be considered for MoS<sub>2</sub>.

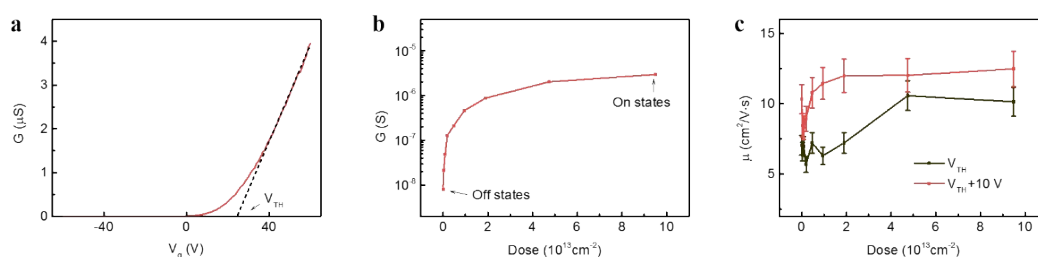


**Fig. S19 e-beam induced doping in MoS<sub>2</sub>.** **a**, determination of threshold voltage from a gate curve. **b**, Dose dependence of MoS<sub>2</sub> conductance at 0 V back gate. **c**, Dose dependence of MoS<sub>2</sub> mobility extracted at threshold voltage ( $V_{TH}$ ) and 10 V away from  $V_{TH}$ .

## Reference

1. L. Zheng, X. Cheng, Z. Wang, C. Xia, D. Cao, L. Shen, Q. Wang, Y. Yu and D. Shen, *J. Phys. Chem. C*, 2015, **119**, 5995-6000.
2. P. Hirsch, M. Kassens, M. Puttmann and L. Reimer, *Scanning*, 1994, **16**, 101-110.
3. D. Teweldebrhan and A. A. Balandin, *Appl. Phys. Lett.*, 2009, **94**, 013101.
4. J. H. Choi, J. Lee, S. M. Moon, Y. T. Kim, H. Park and C. Y. Lee, *Journal of Physical Chemistry Letters*, 2016, **7**, 4739-4743.
5. J. H. Chen, W. G. Cullen, C. Jang, M. S. Fuhrer and E. D. Williams, *Phys. Rev. Lett.*, 2009, **102**, 236805.
6. A. C. Ferrari, *Solid State Commun.*, 2007, **143**, 47-57.
7. M. Azzolini, T. Morresi, G. Garberoglio, L. Calliari, N. M. Pugno, S. Taioli and M. Dapor, *Carbon*, 2017, **118**, 299-309.
8. Y. Y. Wang, Z. H. Ni, T. Yu, Z. X. Shen, H. M. Wang, Y. H. Wu, W. Chen and A. T. S. Wee, *J. Phys. Chem. C*, 2008, **112**, 10637-10640.
9. D. Drouin, A. R. Couture, D. Joly, X. Tastet, V. Aimez and R. Gauvin, *Scanning*, 2007, **29**, 92-101.
10. E. Schreiber and H. J. Fitting, *Journal of Electron Spectroscopy and Related Phenomena*, 2002, **124**, 25-37.
11. Y. B. Zhou, D. S. Fox, P. Maguire, R. O’Connell, R. Masters, C. Rodenburg, H. C. Wu, M. Dapor, Y. Chen and H. Z. Zhang, *Sci. Rep.*, 2016, **6**, 21045.

12. J. H. Chen, C. Jang, M. Ishigami, S. Xiao, W. G. Cullen, E. D. Williams and M. S. Fuhrer, *Solid State Commun.*, 2009, **149**, 1080-1086.
13. S. Adam, E. H. Hwang, V. M. Galitski and S. Das Sarma, *P. Natl. Acad. Sci. USA*, 2007, **104**, 18392-18397.
14. I. Childres, L. A. Jauregui, M. Foxe, J. Tian, R. Jalilian, I. Jovanovic and Y. P. Chen, *Appl. Phys. Lett.*, 2010, **97**, 173109.
15. G. Liu, D. Teweldebrhan and A. A. Balandin, *IEEE Transactions on Nanotechnology*, 2011, **10**, 865-870.
16. M. Z. Hossain, S. Rumyantsev, M. S. Shur and A. A. Balandin, *Appl. Phys. Lett.*, 2013, **102**, 153512.
17. M. Z. Iqbal, O. Kelekci, M. W. Iqbal and J. Eom, *Carbon*, 2013, **59**, 366-371.
18. X. Yu, Y. Shen, T. Liu, T. Wu and Q. Jie Wang, *Sci. Rep.*, 2015, **5**, 12014.
19. Y. H. He, L. Wang, X. L. Chen, Z. F. Wu, W. Li, Y. Cai and N. Wang, *Appl. Phys. Lett.*, 2011, **99**, 033109.